Eur. Phys. J. A (2026) 62:109
https://doi.org/10.1140/epja/s10050-026-01869-6

THE EUROPEAN PHYSICAL JOURNAL A

Regular Article - Experimental Physics

Performances of a $SrI_2(Eu)$ crystal scintillator and its application to the search of ^{84}Sr $\beta\beta$ decay

A. Giarnetti[1], P. Belli[2,3], R. Bernabei[2,3,a], F. Cappella[1], V. Caracciolo[2,3], R. Cerulli[2], A. Incicchitti[1,4], A. Leoncini[2,3], V. Merlo[2], S. Nisi[5]

[1] INFN Sezione di Roma, Rome 00185, Italy
[2] INFN Sezione di Roma "Tor Vergata", Rome 00133, Italy
[3] Dipartimento di Fisica, Universitá di Roma "Tor Vergata", Rome 00133, Italy
[4] Dipartimento di Fisica, Universitá di Roma "Sapienza", Rome 00185, Italy
[5] INFN, Laboratori Nazionali del Gran Sasso, Assergi (AQ) 67100, Italy

Received: 20 March 2026 / Accepted: 23 April 2026

Communicated by Robert Janssens

Abstract A new strontium iodide crystal doped by europium ($SrI_2(Eu)$; mass $\simeq 130$ g) was produced by selected materials using the vertical Bridgman method. It was measured over 4140 h deep underground at the Gran Sasso National Laboratory (LNGS) of the INFN in the DAMA/CRYS low-background set-up. A characterization of the crystal features and performances has preliminarily been investigated. The obtained results have been used in the search for the double electron capture and electron capture with positron emission in ^{84}Sr; new and improved limits have been achieved for these processes, with half-lives $T_{1/2}$ reaching the level of several 10^{17} yr. Further improvements of low background techniques in the $SrI_2(Eu)$ crystal development would offer additional increase of reachable experimental sensitivities on ^{84}Sr $\beta\beta$ decay modes.

Contents

[a] e-mail: rita.bernabei@roma2.infn.it (corresponding author)

1 Introduction

The interest in the strontium iodide europium doped crystal as a scintillator (originally pointed out by Hofstadter in [1]) is increased at some extent because of its high light output and, thus, good energy resolution (FWHM $\approx 3\%$ at 662 keV [2]). Its features have been investigated by several authors, both to achieve a detailed understanding of its performances and to identify potential strategies for improvement (see, e.g., Refs. [2–12]).

$SrI_2(Eu)$ scintillators are promising for various applications, particularly for low-counting experiments such as searches for $\beta\beta$ decay [7]. Compared with other high-resolution scintillators, e.g., $LaCl_3(Ce)$, $LaBr_3(Ce)$, $Lu_2SiO_5(Ce)$, and $LuI_3(Ce)$, $SrI_2(Eu)$ does not contain naturally occurring long-lived radioactive isotopes, such as those present in lanthanum or ^{176}Lu in lutetium.

In the present work, following the initial interest expressed in Ref. [7] in investigating some $\beta\beta$ decay modes of ^{84}Sr, the effective "source = detector" approach is exploited with a high-resolution scintillator realized within the framework of the INFN Grant 73/Rebus (Dr. F. Cappella). The goal was the realization of a first low-background $SrI_2(Eu)$ crystal scintillator to be installed deep underground at LNGS in the DAMA/CRYS low-background set-up.

In this paper, we first describe the development of the new $SrI_2(Eu)$ crystal scintillator and the experimental setup. The adopted calibration procedures are then presented. The scintillation decay times are measured, and the absence of

Published online: 02 June 2026

Table 1 Contaminants' concentrations in the original SrI_2 and EuI_2 powders before purification and SrI_2(Eu) crystal growth as measured by HR-ICP-MS

Nuclide	SrI_2 (ppb)	EuI_2 (ppb)
^{39}K	< 700	< 1000
^{59}Co	< 3	6
^{133}Cs	42	250
^{139}La	200	2000
^{175}Lu	< 20	< 20
^{208}Pb	70	56
^{232}Th	< 0.15	0.44
^{238}U	< 0.05	< 0.1

pulse shape discrimination (PSD) capability is further confirmed. The radioactive contamination of the crystal is thoroughly investigated using several complementary analysis techniques to characterize the detector and construct a comprehensive model of the residual background. This model is subsequently used to derive new lower limits on the two-neutrino and neutrino-less modes of the $\epsilon\beta^+$ and 2ϵ processes in ^{84}Sr, considering transitions both to the ground state (0^+) and to the first excited state (2^+ at 881.6 keV) of the daughter nucleus ^{84}Kr.

2 Development of the SrI_2(Eu) crystal scintillator

A single crystal of strontium iodide doped by 1.0(3)% of Eu[1] was grown using the vertical Bridgman method [13] in the Radiation Monitoring Devices, Inc. (RMD) company in USA with SrI_2 and EuI_2 powder originally selected within the Rebus activity, and then purified in the company. The contaminant concentrations in the selected SrI_2 and EuI_2 powders, prior to the company's purification process and the growth of the SrI_2(Eu) crystal, are reported in Table 1. These concentrations were determined by High-Resolution Inductively Coupled Plasma Mass Spectrometry (HR-ICP-MS) using 0.692 g of SrI_2 (diluted to 10 mL, 1:100 dilution) and 0.709 g of EuI_2 (diluted to 10 mL, 1:100 dilution). Before the crystal growth, the powders were purified by the company using the zone-refining method with specially designed high-purity boats and dedicated cleaning processes developed for low-radioactivity background applications. The crystal growth was carried out in a crucible made of high-purity fused silica (synthetic quartz), which was also specifically cleaned to meet stringent radiopurity requirements. The crystal was cut into a cylindrical shape from the boule, then polished, and its surfaces were cleaned using procedures developed by the company to minimize surface contamination. This process included final cleaning and packaging in a radon-free glovebox. Finally, due to its hygroscopic nature, the crystal was surrounded by foam and sealed in a hermetic copper housing (⌀3.2 × 5.8 cm) with a quartz window. Packaging component – including the diffuser/reflector, optical coupling, and epoxy – were carefully selected and prepared through collaboration between the company and Rebus. Further HR-ICP-MS measurements of the contaminations in the tip and tail samples of the grown SrI_2(Eu) crystal boule have also been carried out (see Table 2).

Table 2 Contaminants' concentrations in samples of the grown SrI_2(Eu) crystal boule (tip and tail) as measured by HR-ICP-MS

Nuclide	Tip Center (ppb)	Tip Ext (ppb)	Tail Center (ppb)	Tail Ext (ppb)
^{39}K	< 150	276	250	760
^{59}Co	< 20	< 20	< 20	< 20
^{133}Cs	64.5	181	90	860
^{139}La	117	151	275	1360
^{175}Lu	0.38	0.25	0.83	6.85
^{208}Pb	77	12	< 10	36
^{232}Th	< 0.1	< 0.1	< 0.1	0.25
^{238}U	< 0.05	< 0.05	< 0.05	< 0.05

Tip Center: center of tip surface (1.49 g in 20 mL dil 100) Tip Ext: lateral part of tip surface (1.87 g in 20 mL dil 100) Tail center: center of tail surface (1.57 g in 20 mL dil 100) Tail Ext: external part of tip surface (1.38 g in 20 mL dil 100)

The exact crystal mass was not measured by RMD prior to encapsulation; therefore, its value was estimated based on the crystal dimensions (⌀2.6(1) × 5.40(5) cm) and density (4.55 g/cm^3), yielding a total mass of 130(10) g.

3 Experimental setup

The SrI_2(Eu) crystal scintillator arrived at LNGS in March 2023 and was immediately stored underground at a depth of about 3.8 km water equivalent. Measurements in the low-background DAMA/CRYS setup [14] commenced in April 2024, allowing sufficient time for the decay of any short-lived contaminants in the materials.

The SrI_2(Eu) crystal was coupled to a Hamamatsu R12669 photomultiplier tube using optical grease, through a plexiglass light guide (3" diameter, 15 cm length; see Fig. 1). A Teflon holder was employed to couple the scintillator crystal to the light guide, ensuring stable and consistent optical contact between the two components. The detector was installed in the DAMA/CRYS low-background setup at LNGS. The

[1] This value has been measured by ICP-MS in samples from the tip and tail of the grown crystal, as sent by the producer. It is worth noting that the Eu concentration in the grown crystal may be lower due to unknown segregation of Eu in SrI_2, and/or to possible presence of a concentration gradient of the Eu in the crystal.

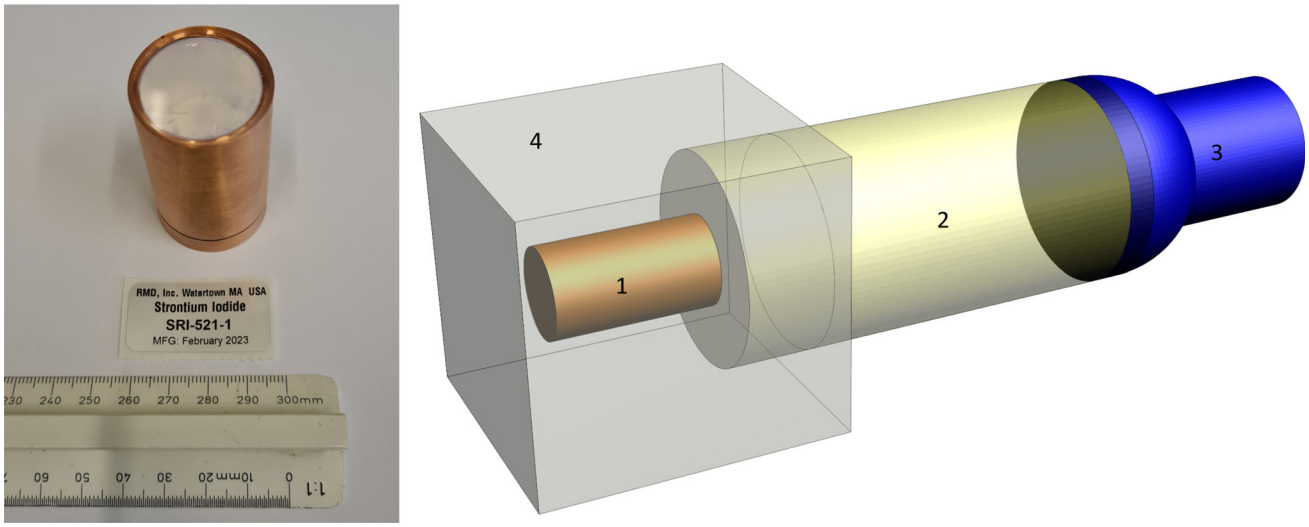

Fig. 1 Left: the $SrI_2(Eu)$ crystal scintillator. Right: scheme of the experimental setup. The number 1 refers to the crystal sealed in its copper housing, 2 is the light guide, 3 is the photomultiplier tube and 4 is a Teflon holder

passive shield of the setup consists of multiple layers of radiopure materials designed to reduce external background: 11 cm of high purity copper, 10 cm of low radioactive lead, 2 mm of cadmium, and 10 cm of polyethylene. The inner volume is continuously flushed with high-purity nitrogen gas to remove environmental radon, while the overburden at LNGS provides substantial suppression of the cosmic-ray flux.

The data acquisition system was based on a 250-M Sample/s 12-bit transient digitized CAEN DT5720B. The trigger was produced by the ORTEC model 454 Timing Filter Amplifier and provided the selection of scintillation events rejecting the photomultiplier tube noises. The waveform of each event was recorded in a 32 μs time window with 4 ns time bins. Given that the $SrI_2(Eu)$ scintillator has a decay time of a few μs [7,9–12], the event amplitude was calculated as the area of the waveform over 2000 channels (8 μs) after baseline subtraction. The integration window was optimized to achieve the best energy resolution in the resulting energy spectrum.

The calibration of the energy scale was performed before the low-background measurement with γ sources introduced into the setup by means of a PTFE pipe, without requiring neither the opening of the setup nor the shut down of the high voltage on the photomultiplier tube, allowing stable conditions during both calibration and data taking.

4 Energy calibration

The energy scale and resolution of the scintillator were measured with three sources before the low-background measurements: ^{133}Ba, ^{60}Co and ^{228}Th. The main peaks of the sources were fitted with Gaussian functions, showing a good linearity (see Fig. 2). The following energy dependence was obtained for the energy resolution:

$$\sigma_\gamma[\text{keV}] = \sqrt{0.2172(17)\, E_\gamma + 2.90(20) \times 10^{-5}\, E_\gamma^2} \quad (4.1)$$

where E_γ is γ-ray quanta energy in keV.
The stability of the detector response during the data taking was controlled observing the γ peaks of the ^{152}Eu contamination of the crystal, in particular the most prominent one at 168.7 keV, as calibration with external radioactive sources was performed only once. A slight shift ($\lesssim 1\%$) of the energy scale was observed during data taking. To compensate this effect the energy was rescaled by a suitable quadratic function in time.

A key aspect of the energy reconstruction is the strong correlation observed between the integrated charge and the pulse mean time, defined as

$$t_m = \sum_{i=i_0}^{i_0+N_w} t_i\, q_i \Big/ \sum_{i=i_0}^{i_0+N_w} q_i\,, \quad (4.2)$$

where i_0 denotes the digitized sample corresponding to the pulse start time t_0, N_w is the width of the integration window (2000 channels, 8000 ns), t_i is the time of the i-th digitized sample, and q_i is the baseline-subtracted pulse amplitude.

Most events clustered around a characteristic mean time (see Sec. 5 and Fig. 3), while a significant fraction exhibited noticeably smaller values of t_m. In particular, the calibration spectra obtained by selecting different t_m windows show that pulses with shorter mean times are systematically assigned higher integrated charge, an effect that becomes more pronounced at higher energies.

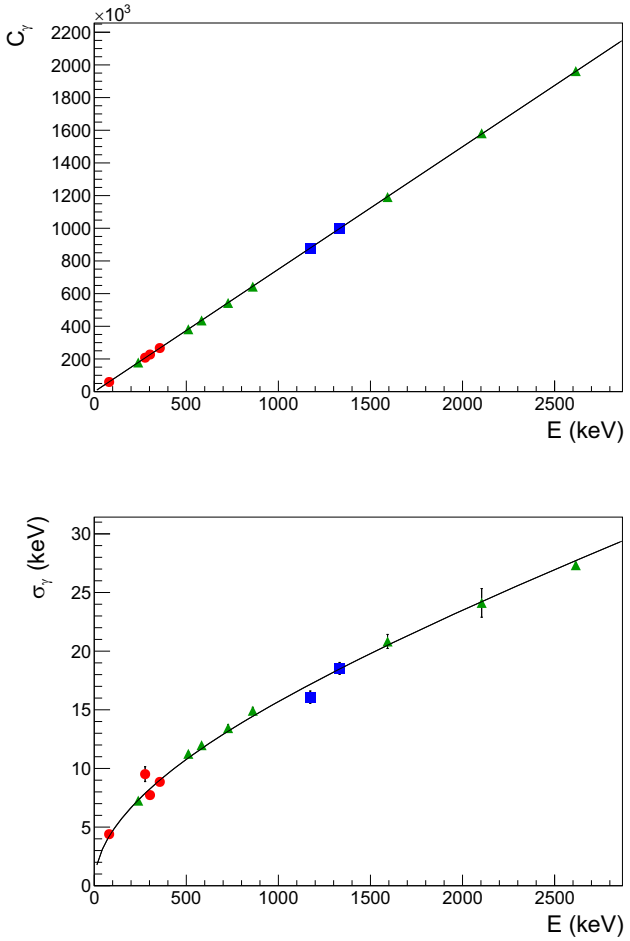

Fig. 2 Linearity (top panel) and energy resolution (bottom panel) obtained from calibration. Red circles correspond to the peaks from ^{133}Ba sources, blue squares from the ^{60}Co source and green triangles from ^{228}Th source

This behavior is attributed to a non-uniform Eu doping in the crystal: in regions with lower europium concentration the pulses are faster, leading to shorter time profiles [10,11], and larger integrated charge within the same limited acquisition window. To correct for this bias, the empirical correction:

$$E_\gamma^c = \frac{E_\gamma}{1 - a\,(t_m - t_m^0)} \tag{4.3}$$

was introduced. Here, E_γ and t_m denote the event energy, as determined from the standard calibration, and the corresponding mean time, respectively. The parameter t_m^0 represents the mode of the mean-time distribution; it is equal to $\sim$ 2780 ns for energies above 100 keV and shows a slight energy dependence below this threshold.

The magnitude of the correction is determined by the parameter a, which was optimized by minimizing the resolution, σ, of the 2614.5 keV ^{208}Tl peak, where the effect is most pronounced due to its proportionality to energy. The optimal value was found to be $a = 1.1 \times 10^{-4}$ ns^{-1}. Note that the final energy calibration reported in Fig. 2 has been obtained after applying this correction.

Finally, the study on the scintillation decay time of the SrI_2(Eu) scintillator is reported in Appendix A.

5 Pulse-shape discrimination

Despite the ongoing development efforts, the SrI_2(Eu) crystal scintillator studied in this work still exhibits significant intrinsic radioactive contamination. Several data-taking runs were performed over a period of approximately six months (for a total live-time of 4140 h) to characterize and identify the contaminant nuclides.

To assess the possibility of discriminating between α particles and β/γ events via pulse-shape differences, the recorded events were displayed in the mean-time versus energy plane (see Fig. 3, left panel). As shown there, the crystal does not exhibit an effective pulse-shape discrimination capability between α and β/γ interactions, in agreement with existing literature [7,8]. Indeed, the mean-time distributions at fixed energy do not show appreciable differences over the full spectrum.

Most of the recorded events lie below 2000 keV. Above this energy, distinct clusters are observed up to approximately 4000 keV, which are attributed to α particles originating from internal crystal contamination.

A detailed analysis of the α spectrum is presented in the following sections. Although the pulse shapes of α and β/γ events are similar and cannot be fully separated, the sparse events above 4000 keV visible in Fig. 3 are identified as fast BiPo sequences from the ^{232}Th decay chain, in which a β decay is immediately followed by an α decay within the same acquisition window. These events are excluded from all subsequent analyses.

The t_m distributions were divided into energy intervals up to 4000 keV. Within each interval, the distribution was fitted with a Gaussian function featuring an exponential tail, and the corresponding 99.73% confidence regions were determined. The resulting boundaries are shown in the figure as red lines, and only events falling within these intervals were retained for the contamination analysis. As previously noted, the mean-time distributions broaden toward lower t_m values due to inhomogeneous Eu doping (see Fig. 3, right panel). In the α-dominated region of the spectrum ($E > 2000$ keV), the t_m distribution becomes even broader. This effect may be related to the localized energy deposition of α particles combined with inhomogeneities in the Eu doping. Therefore, in the subsequent analyses, the lower bound on t_m for $E > 2000$ keV was conservatively removed.

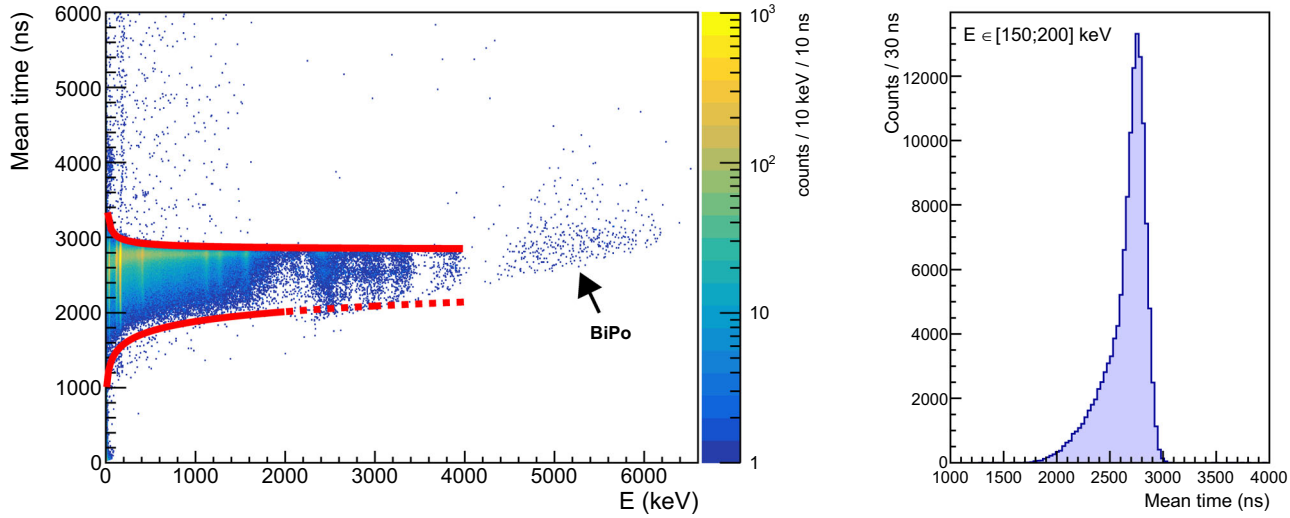

Fig. 3 Left panel: scatter plot regarding all the detected events during the 4140 h of data taking in the E - t_m plane. The red lines, used for the event selection in the subsequent analyses, depict the mean time interval containing 99.73% of the data. For $E > 2000$ keV the lower bound (dashed line) was removed, see text for details. Right panel: mean time distribution of events with energy between 150 and 200 keV

6 Radioactive contamination of the crystal

Understanding the sources of background radiation in the $SrI_2(Eu)$ detector is required for interpreting data in the region of interest for ^{84}Sr $\beta\beta$ decay. The energy spectrum accumulated over approximately six months (4140 h) of measurements is shown in Fig. 4. It exhibits several distinct features: a broad β-decay continuum with prominent γ-ray peaks below 2000 keV, and a characteristic α-particle population between roughly 2000 keV and 4000 keV.

The dominant background contributions arise from radio active impurities in the crystal and the photomultiplier tube. All other components of the low-background setup were built from carefully selected materials with minimal radioactivity, resulting in a negligible impact on the overall background.

To quantify the radioactive impurities in the $SrI_2(Eu)$ scintillator, several analytical methods were employed: Monte Carlo modelling of α and combined β/γ energy spectra, temporal analysis of fast decay sequences within the ^{232}Th, ^{238}U and ^{235}U decay series (time-amplitude analysis). The detector's response characteristics to various radionuclide decay processes were modelled using Monte Carlo simulations performed with the Geant4 toolkit [15], package version 10.06.p01; the Livermore physics list was used to describe the electromagnetic interactions.

6.1 Time-amplitude analyses

Time-amplitude analyses were performed to identify fast decay sequences within the ^{232}Th, ^{235}U, and ^{238}U decay chains, exploiting the arrival time and energy of each recorded event. The three investigated sub-chains are:

- **^{228}Th sub-chain** (^{232}Th): ^{224}Ra ($Q_\alpha = 5.79$ MeV, $T_{1/2} = 3.66$ d) $\rightarrow$ ^{220}Rn ($Q_\alpha = 6.40$ MeV, $T_{1/2} = 55.6$ s) $\rightarrow$ ^{216}Po ($Q_\alpha = 6.91$ MeV, $T_{1/2} = 144$ ms) $\rightarrow$ ^{212}Pb.
- **^{227}Ac sub-chain** (^{235}U): ^{223}Ra ($Q_\alpha = 5.98$ MeV, $T_{1/2} = 11.44$ d) $\rightarrow$ ^{219}Rn ($Q_\alpha = 6.95$ MeV, $T_{1/2} = 3.96$ s) $\rightarrow$ ^{215}Po ($Q_\alpha = 7.53$ MeV, $T_{1/2} = 1.781$ ms) $\rightarrow$ ^{211}Pb.
- **^{226}Ra sub-chain** (^{238}U): ^{214}Bi ($Q_\beta = 3.27$ MeV, $T_{1/2} = 19.7$ min) $\rightarrow$ ^{214}Po ($Q_\alpha = 7.83$ MeV, $T_{1/2} = 164$ μs) $\rightarrow$ ^{210}Pb.

For each sub-chain, specific time intervals (based on the half-lives) and energy windows were applied to each decay to identify genuine decay sequences while suppressing random coincidences and backgrounds from other chains. The low-energy bounds on the α peaks also remove a population of degraded α's from possible surface contamination, contributing, for example, approximately 15% of the total events in the ^{228}Th analysis. The selection criteria and their efficiencies are summarised in Table 3. The energy spectra of the selected events are shown in Fig. 5, where the distinct α peaks of each decay sequence are clearly visible. The half-lives extracted from exponential fits to the measured inter-event time distributions are in good agreement with the literature, providing a valuable cross-check of the analysis (see Table 3). The activities obtained after correct-

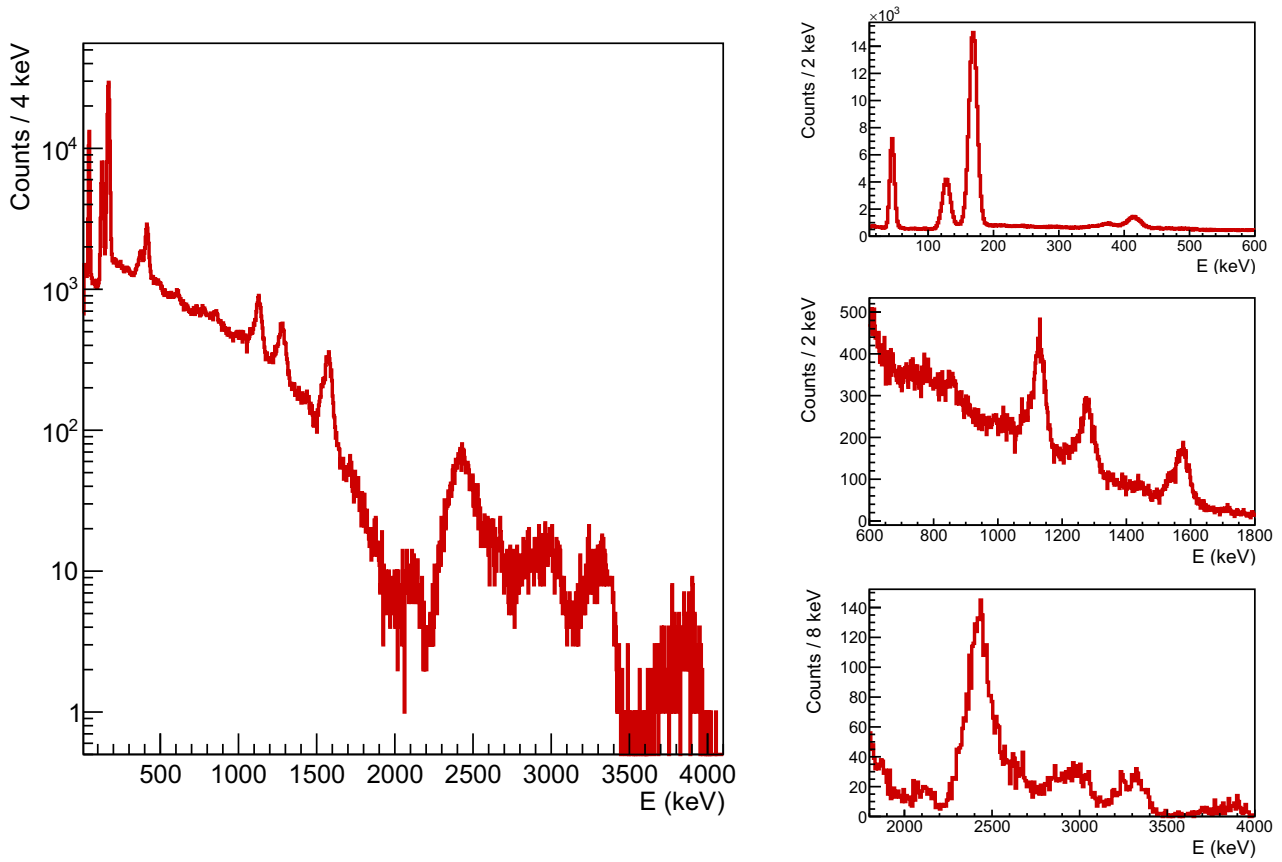

Fig. 4 Energy spectrum of the $SrI_2(Eu)$ crystal detector accumulated over 4140 h of measurements. The main panel shows the full spectrum from 0 to 4000 keV on a logarithmic scale, highlighting both the low-energy β/γ continuum and the high-energy α region. Three inset panels provide expanded views of selected energy ranges: the energy regions (10–600 keV) and (600–1800 keV), dominated by β decay and characteristic γ ray peaks from ^{152}Eu and other radioactive contaminants; and the high-energy region (2000–4000 keV), showing multiple α decay peaks associated with natural radioactive decay chains

ing for selection efficiencies are 0.293(13) mBq/kg for the ^{228}Th sub-chain, 0.022(4) mBq/kg for the ^{227}Ac sub-chain, and 0.107(8) mBq/kg for the ^{226}Ra sub-chain.

6.2 α quenching factor determination

Using the identified α peaks from the ^{232}Th, ^{235}U and ^{238}U decay chains, the quenching factor for α particles in the $SrI_2(Eu)$ crystal was determined. Figure 6 illustrates the dependence of the quenching factor, defined as $\alpha/\beta = E_{\text{rec}}/E_\alpha$, on E_α, where E_{rec} is the reconstructed energy in keV electron equivalent and E_α is the nominal α energy. The contribution of the nuclear recoil following the α decay has been accounted for in E_{rec} assuming a nuclear quenching factor of 10%. Only α transitions with ground state branching ratios exceeding 95% were included in the analysis, thereby excluding peaks for which a significant fraction of decays is accompanied by unquenched γ ray emission. In particular, the ^{223}Ra and ^{219}Rn peaks were omitted from this preliminary study due to substantial feeding of excited states (99% and 21%, respectively).

A slight saturation effect was observed in the pulses of events with reconstructed energies above 3000 keV electron equivalent. This effect becomes significant in the ^{214}Po peak region, resulting in an underestimation of the corresponding effective α/β ratio. A linear fit was therefore performed using only the first four data points. The fit, shown as the red line in Fig. 6, yields:

$$\alpha/\beta = 0.347(6) + 2.05(10) \times 10^{-5} E_\alpha, \tag{6.1}$$

where E_α is the energy of the α particle in keV. This preliminary determination serves as a cross-check of the full Monte Carlo fit. For comparison, the green line represents the quenching relation obtained from the comprehensive Monte Carlo analysis described below, which incorporates all available α peaks and yields a more precise determination of the quenching behavior.

Table 3 Summary of the time-amplitude analyses for the ^{228}Th (^{232}Th chain), ^{227}Ac (^{235}U chain), and ^{226}Ra (^{238}U chain) sub-chains. For each transition the inter-event time window Δt with its corresponding selection efficiency ε, the energy window applied to the relevant events, and the half-life $T_{1/2}$ obtained from an exponential fit to the inter-event time distribution are reported. To account for the acquisition window duration, a lower bound of 40 μs was applied to the Δt windows. The total number of identified coincidences N_{coinc} and the resulting activity (corrected for selection efficiencies) are given per sub-chain

Sub-chain	Transition	Δt	ε (%)	Energy window (keV)	$T_{1/2}$	N_{coinc}	Activity (mBq/kg)
^{228}Th	^{220}Rn $\rightarrow$ ^{216}Po	4 min	95.0	^{224}Ra:[2450, 2850] ^{220}Rn:[2750, 3200]	59(5) s	512	0.293(13)
	^{216}Po $\rightarrow$ ^{212}Pb	620 ms	95.0	^{216}Po: [3100, 3500]	144(10) ms		
^{227}Ac	^{219}Rn $\rightarrow$ ^{215}Po	18 s	95.7	—	7(3) s	37	0.022(4)
	^{215}Po $\rightarrow$ ^{211}Pb	6 ms	90.3	^{215}Po: > 3400	1.3(3) ms		
^{226}Ra	^{214}Bi $\rightarrow$ ^{214}Po	700 μs	79.3	^{214}Bi:[10, 3000]^{214}Po: > 3500	176(21) μs	165	0.107(8)

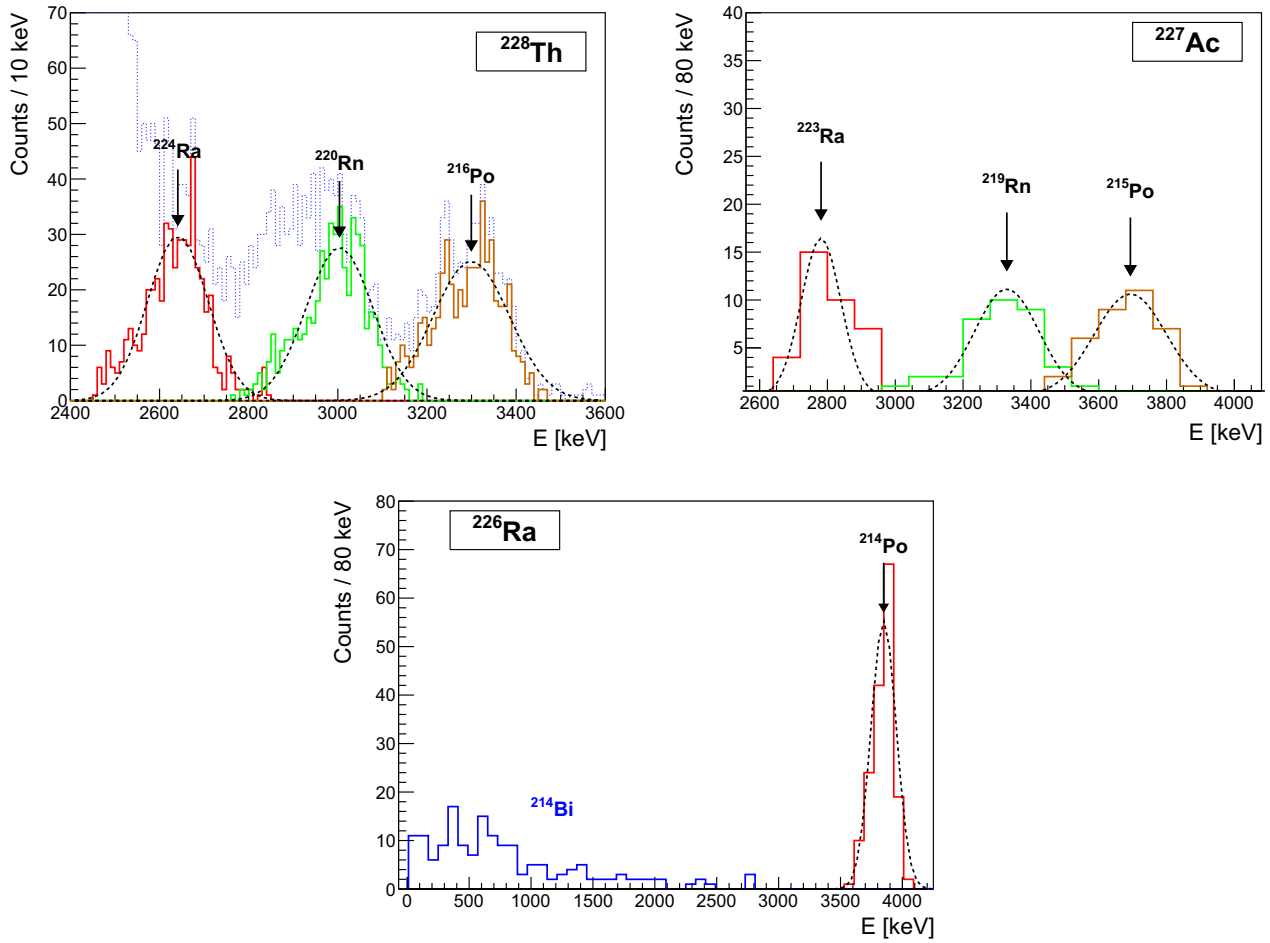

Fig. 5 Energy spectra of events selected via time-amplitude analysis for the three investigated sub-chains. Top left: ^{228}Th sub-chain, showing α peaks from ^{224}Ra, ^{220}Rn, and ^{216}Po overlaid on the full spectrum (blue dotted histogram); dashed lines show Gaussian fits. Top right: ^{227}Ac sub-chain, showing α peaks from ^{223}Ra, ^{219}Rn, and ^{215}Po and the Gaussian fits (dashed lines). Bottom: ^{226}Ra sub-chain, displaying the ^{214}Bi β continuum and the ^{214}Po α peak with Gaussian fit (dashed line). In all panels the energy scale is calibrated with γ-sources

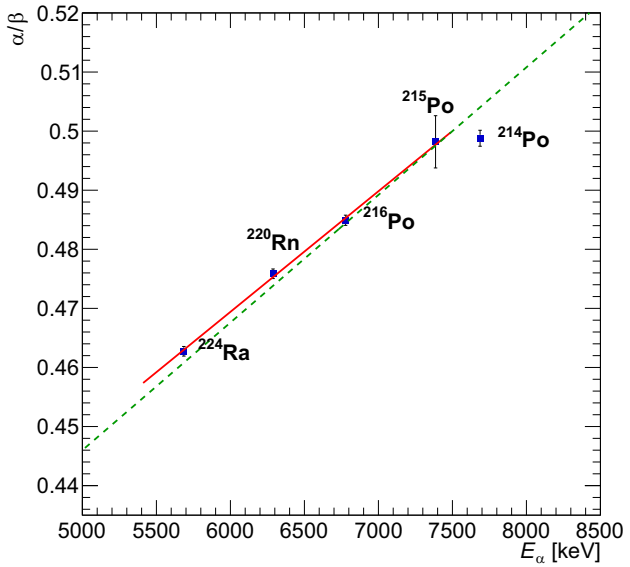

Fig. 6 Quenching factor $\alpha/\beta = E_{\rm rec}/E_\alpha$ as a function of true α energy. The black points represent α peaks identified by time-amplitude analysis, with ground state branching ratios exceeding 95%. The red line shows a linear fit excluding the ^{214}Po peak (see text for details). The green line indicates the result from the full Monte Carlo fit described in the text, which incorporates all identified α peaks and provides a more comprehensive characterization of the energy-dependent quenching behavior

6.3 Study of the α contaminants

Since the SrI_2(Eu) scintillator does not provide effective pulse-shape discrimination between α particles and β/γ events, the analysis of the α spectrum has been performed simply selecting the energy region above 2000 keV, where α events dominate the spectrum, up to approximately 4100 keV. This energy selection allowed for a clean separation of α events from the β/γ background, enabling a suitable characterization of the α emitting contaminants through spectral analysis.

A comprehensive fit of the α spectrum was performed using Monte Carlo simulations based on the Geant4 toolkit. The simulated spectrum, shown in Fig. 7 together with the experimental data, includes all α decays originating from crystal contaminants ^{238}U, ^{232}Th, and ^{235}U. Secular equilibrium in the ^{238}U, ^{232}Th, and ^{235}U decay chains was assumed to be broken; therefore, each chain was divided into sub-chains considered to be in internal equilibrium. The activities of the sub-chains ^{234}U$\rightarrow^{230}$Th, ^{230}Th$\rightarrow^{226}$Ra, ^{226}Ra$\rightarrow^{210}$Pb, ^{210}Pb$\rightarrow^{206}$Pb, ^{228}Th$\rightarrow^{208}$Pb, ^{231}Pa$\rightarrow^{227}$Ac, and ^{227}Ac$\rightarrow^{207}$Pb were treated as free parameters of the fit.[2]

[2] The other U and Th sub-chains (^{238}U$\rightarrow^{234}$U, ^{232}Th$\rightarrow^{228}$Ra, ^{228}Ra$\rightarrow^{228}$Th, and ^{235}U$\rightarrow^{231}$Pa) mostly populate the energy region below 2000 keV and will be investigated in the next section.

The quenching of α particles was implemented using a linear model as in Eq. 6.1, with parameters optimized during the fit. The α particle energy resolution, which differs from that of β/γ events due to their distinct ionization properties, was parameterized as:

$$\sigma_\alpha = \sqrt{a + b\,E}. \tag{6.2}$$

The pulse saturation effect described in the previous section, evaluated to be approximately 0.7% at the ^{214}Po α peak, was parameterized and implemented in the simulation as a correction to the energy for $E > 3030$ keV.

The Monte Carlo simulation included the full detector geometry, material composition, and radioactive decay schemes. For each decay chain, the simulation accounted for the emission of α particles, accompanying γ rays, and conversion electrons, as well as their transport through the crystal and the resulting energy deposition. The fit, performed over the energy range (2040–4100) keV, yielded χ^2/NDF = 1.17, indicating good agreement between the model and data across the entire α energy range. The fitted spectrum, shown as red curve in Fig. 7, reproduces well the observed peak positions and relative intensities. The activities of the α emitting contaminants extracted from this fit are consistent with those reported in Table 4, which were obtained from a fit to the full spectrum, including β/γ contaminants (see next section). Furthermore, these results are also in agreement with the activities independently determined through the time-amplitude analyses for the ^{228}Th, ^{227}Ac, and ^{226}Ra sub-chains, providing strong validation of both analysis methods. The individual contributions from each decay chain are also shown in the figure, illustrating the complexity of the α background and the potentiality of the Monte Carlo approach in disentangling overlapping spectral features. The best fit of the α quenching is compatible within one standard deviation with the value obtained from the time-amplitude analysis:

$$\alpha/\beta = 0.338(2) + 2.16(4) \times 10^{-5}\,E_\alpha, \tag{6.3}$$

where E_α is the energy of the α particle in keV. A good consistency was also observed between the Gaussian widths extracted from the fits of the time-amplitude peaks and the best fit energy resolution of the α spectrum:

$$\sigma_\alpha[\text{keV}] = \sqrt{1.63(9)\,E}, \tag{6.4}$$

where E is the energy of the α particle in keV electron equivalent.

6.4 Study of the β/γ contaminants

Following the characterization of the α contamination, a comprehensive fit of the full energy spectrum was performed

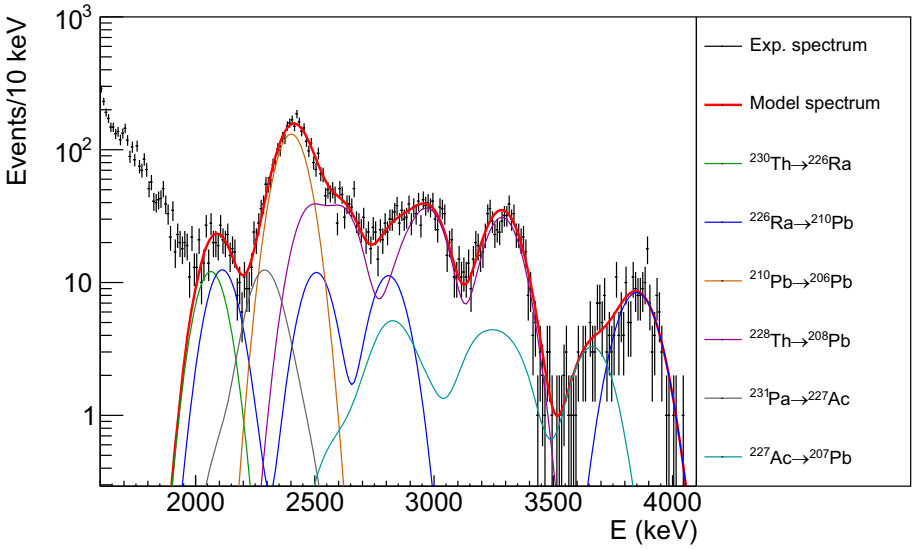

Fig. 7 Monte Carlo fit of the α spectrum. Black points denote the experimental data, and the red curve shows the total fitted model. Colored curves display the contributions from the individual decay chains

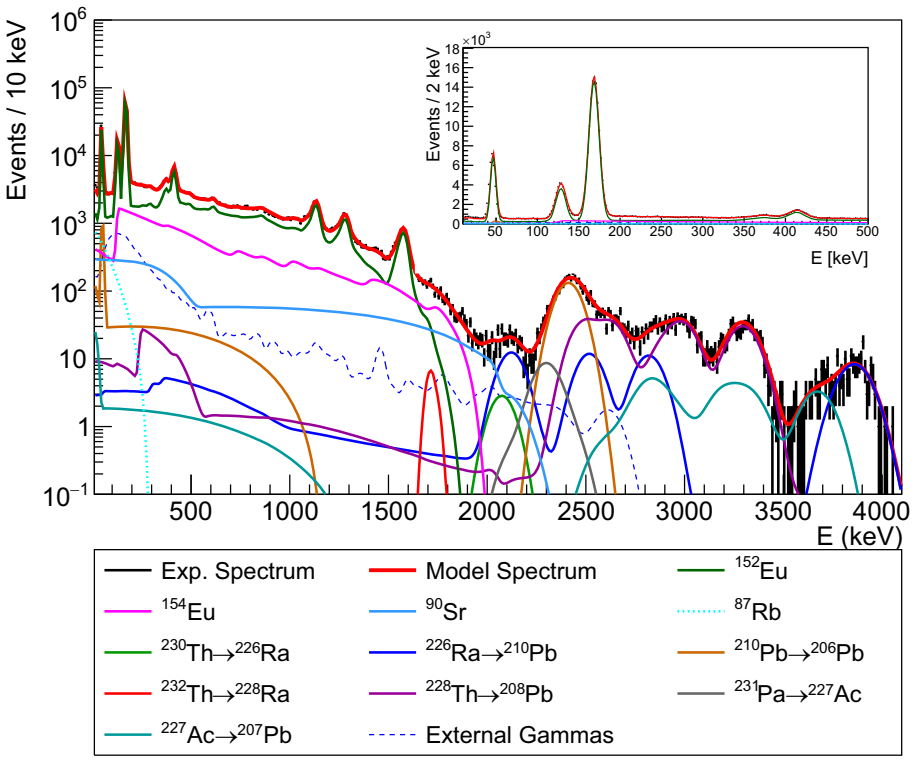

Fig. 8 Monte Carlo fit of the full energy spectrum (see text for details). The black points represent the experimental data, and the red curve shows the total fitted model. Colored curves show individual contributions from different sources. In the inset, a zoom of the low-energy region is shown in linear scale

to identify and quantify the β and γ emitting contaminants. The fit was performed over the energy range (66–4100) keV. Due to a slight non-linearity observed in the detector response up to 148 keV, only the energy range between 66 and 112 keV was included in the fit below this threshold. This interval was selected because it contains no peaks and the impact of the non-linearity is negligible. To compensate for reduced statistics at higher energies, a coarser binning was applied above 1700 keV (10 keV per bin instead of 2 keV), where the number of recorded events was significantly lower. The results are shown in Fig. 8, which displays the measured spectrum, the total fitted model, and the contributions from individual components.

The dominant β/γ activity was attributed to ^{152}Eu contamination, identified through its characteristic γ ray peaks. The presence of ^{152}Eu likely originates from neutron activation of naturally occurring ^{151}Eu; its activity depends on the history of the materials used for the production of the crystal. Additional contamination from ^{154}Eu was also identified and included in the model. A significant contribution from ^{90}Sr was observed, particularly affecting the mid-energy region

Table 4 Activities of α and β/γ emitting contaminants were determined from a Monte Carlo fit of the spectrum. Limits are quoted at the 90% confidence level. The ^{234}U and ^{230}Th peaks cannot be resolved individually due to their very similar spectra; therefore, their activities are reported together

Chain	Nuclide	Activity (mBq/kg)
^{238}U	^{238}U	< 0.02
	^{234}U + ^{230}Th	0.022(16) [a]
	^{226}Ra	0.098(7) [a]
	^{210}Pb	1.07(3) [a]
^{235}U	^{235}U	< 0.06
	^{231}Pa	0.08(2) [a]
	^{227}Ac	0.033(4) [a]
^{232}Th	^{232}Th	0.022(16)
	^{228}Ra	< 0.7
	^{228}Th	0.288(9) [a]
	^{152}Eu	191.8(6)
	^{154}Eu	39.2(9)
	^{90}Sr	4.6(3)
	^{87}Rb	3.2(5)
	^{40}K	< 0.17

([a]) The parameter's initial value was determined from the fit to the α spectrum

of the spectrum through its β decay ($Q_\beta = 546$ keV) and the subsequent β decay of its daughter ^{90}Y ($Q_\beta = 2279$ keV).

To accurately describe the low-energy region ($E < 200$ keV), contamination from ^{87}Rb was included in the fit. The presence of ^{87}Rb in the crystal may originate from trace impurities in the strontium source material or in the growth equipment during crystal production. Additionally, natural rubidium contains roughly 27.8% of the β emitting isotope ^{87}Rb, which has an extremely long half-life of 4.97×10^{10} yr. Even trace amounts of this isotope can be detected over extended measurement periods. The β decay of ^{87}Rb to ^{87}Sr has an endpoint energy of 282 keV, contributing predominantly to the low-energy part of the spectrum.

External γ ray contributions from the photomultiplier tube were incorporated into the model to explain spectral features not arising from internal crystal contamination. These external γ rays primarily originate from ^{40}K and uranium/thorium chain isotopes in the glass and ceramic components of the photomultiplier tube.

The energy resolution function used for the γ ray calibration measurements was applied to all simulated β and γ spectra. The fit returned as best fit

$$\sigma_\gamma[\text{keV}] = \sqrt{0.2223(18)E_\gamma + 2.8(5) \times 10^{-5}E_\gamma^2} \qquad (6.5)$$

where E_γ is in keV. This result is compatible with the resolution obtained during the calibration phase. For energies above 2000 keV, both the α quenching factor and the α energy resolution (Eq. 6.3 and Eq. 6.4) obtained from the α spectrum analysis were fixed to their previously determined values. The fit parameters associated with the activities of the α emitting contaminants were initialized using the values obtained from the α spectrum fit.

The fit converged with χ^2/NDF = 1.6, demonstrating agreement between the model and the measured spectrum across the entire energy range. Table 4 lists the fitted activities for all β/γ and α emitting contaminants along with their uncertainties obtained with the full spectrum fit. The activities of ^{226}Ra, ^{210}Pb, ^{227}Ac, and ^{228}Th are consistent with the results from the α spectrum and time-amplitude analyses. In contrast, for ^{230}Th/^{234}U and ^{231}Pa, the presence of a tail from some β/γ contaminants in the α energy region results in slightly lower fitted activities compared to the α-spectrum fit shown in Fig. 7.

7 Results on $\beta\beta$ decay modes of ^{84}Sr

The experimental setup and the high light yield of the SrI_2(Eu) crystal provide a unique opportunity to investigate rare nuclear processes in Strontium isotopes, particularly the $\beta\beta$ decay processes in ^{84}Sr. Naturally occurring strontium contains ^{84}Sr with an isotopic abundance of 0.56(2)% [16]. The Q-value for the double electron capture in ^{84}Sr is 1790.115(37) keV [17]. Five distinct decay channels were specifically considered: the two-neutrino (2ν) and the neutrinoless (0ν) modes for $\varepsilon\beta^+$ and 2ε processes, targeting both the ground state (0^+) and the first excited level (2^+ at 881.6 keV) of the daughter nucleus ^{84}Kr.

To investigate these processes, extensive Monte Carlo simulations were performed using the Geant4 toolkit and the DECAY0 event generator [18]. For each rare process, the specific decay kinematics and the subsequent atomic and nuclear de-excitations occurring within the crystal volume were modelled. The resulting energy depositions were processed to account for the detector's energy resolution.

The statistical analysis followed a strategy analogous to the one employed for the β/γ background fit. The fit was performed in the energy range from 66 to 4100 keV, with the (112–148) keV region excluded to avoid local non-linearities. The background model, consisting of all identified internal and external radioactive contaminants, served as a baseline. The simulated spectrum for each rare process was added to this background model individually as a free parameter. No features attributable to any of the $\beta\beta$ processes in ^{84}Sr were observed in the measured energy spectrum.

To determine the confidence intervals for the number of events (S) associated with each process, the Feldman-

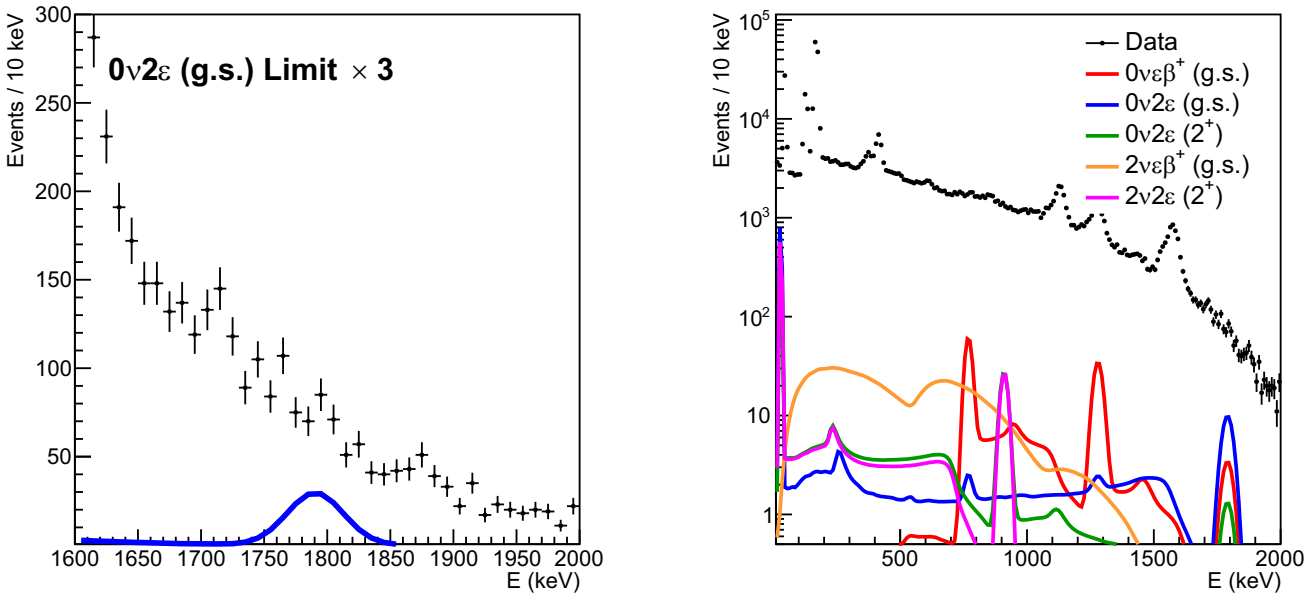

Fig. 9 Determination of the 90% C.L. upper limits for $\beta\beta$ processes in ^{84}Sr. The left panel shows the experimental spectrum (black points) around the most prominent peak of the $0\nu 2\varepsilon$ transition to the ground state of the daughter nucleus, with the excluded signal depicted in blue and amplified by a factor of 3 for visibility. The right panel shows the excluded signals for all five decay channels, each normalized to its limS value

Table 5 Lower limits on the half-lives ($T_{1/2}$) at 90% C.L. for various $\beta\beta$ decay processes in ^{84}Sr

Process	Decay mode	Level of daughter	$T_{1/2}$ Limit (This work)[yr]	Past Limits [7][yr]
$\varepsilon\beta^+$	0ν	g.s. (0^+)	$> 6.0 \times 10^{17}$	$> 6.9 \times 10^{15}$
$\varepsilon\beta^+$	2ν	g.s. (0^+)	$> 2.2 \times 10^{17}$	$> 6.9 \times 10^{15}$
2ε	0ν	g.s. (0^+)	$> 2.9 \times 10^{17}$	$> 1.9 - 6.0 \times 10^{16}$
2ε	0ν	881.6 keV (2^+)	$> 4.9 \times 10^{17}$	$> 2.6 \times 10^{16}$
2ε	2ν	881.6 keV (2^+)	$> 3.6 \times 10^{17}$	$> 3.1 \times 10^{16}$

Cousins unified approach [19] was applied to obtain 90% C.L. upper limits. These event limits were then translated into lower limits on the half-lives ($T_{1/2}$) using the standard formula:

$$T_{1/2} > \ln 2 \cdot \frac{N \cdot T}{\text{limS}} \tag{7.1}$$

where N is the number of ^{84}Sr nuclei in the crystal, estimated to be $1.28(11) \times 10^{21}$, T is the live time (4140 h), and limS is the 90% C.L. upper limit on the number of events. Note that the detection efficiency is intrinsically accounted for within the simulation framework used to generate the signal spectra.

An example of this procedure is illustrated in Fig. 9. The left panel provides a magnified view of most prominent peak in the $0\nu 2\varepsilon$ transition to the ground state of the daughter nucleus. The result of the fit yielded to $S = 300(700)$, limS = 1450 and $T_{1/2} > 2.9 \times 10^{17}$ yr. The excluded signal (blue curve) corresponding to this value of limS is amplified by a factor of 3 for visibility.

The right panel of the figure displays the experimental energy spectrum superimposed with the 90% C.L. excluded signals for all considered ^{84}Sr decay channels.

As a consistency check, upper limits on S were also evaluated using the one-sigma approach, which considers only the most prominent peak for each process without a full background fit; the results were found to be consistent with the comprehensive fit values where applicable. The final results of this search are summarized in Table 5, where they are compared with previous experimental limits from Ref. [7].

The sensitivity to these rare processes has been significantly enhanced by using a high-performance SrI_2(Eu) detector in low-background environment and the "source=detector" approach. Compared to previous experimental work [7], which employed an external HPGe detector

for measurement, the half-life limits were improved across all considered channels.

The most significant improvement was observed in the $0\nu\varepsilon\beta^+$ channel. In the previous study [7], this process was investigated by searching for the annihilation γ rays of positrons, escaping the crystal. In the present work, the "source = detector" approach, enabled by the use of this scintillator crystal, allows the full energy deposition of the emitted positron to be measured, substantially increasing both the detection efficiency and the overall sensitivity of the setup. However, the moderate energy resolution of the scintillator, compared to germanium detectors, prevents distinguishing electron capture events from different electronic shells.

8 Conclusions

A new SrI_2(Eu) crystal scintillator (mass 130(13) g) from selected and purified powders has been realised by vertical Bridgeman technique by the RMD company under supervision of Dr. F. Cappella in the framework of his INFN Grant 73/Rebus. At arrival the SrI_2(Eu) crystal was stored underground within DAMA installations over about one year to allow the decay of possible short/medium life contaminants. The performances of the detector and the investigations on double beta decay modes in ^{84}Sr were then studied deep underground in the low-background DAMA/CRYS set-up.

In this paper the detector performances and the nature of the peaks observed in the experimental energy spectrum have been investigated in detail. The dominant residual background arises from ^{152}Eu, representing a contamination significantly different from that reported in Ref. [7]. From the perspective of developing lower-background SrI_2(Eu) detectors, this highlights the need for further purification efforts of rare-earth elements, in particular ^{152}Eu, in the EuI powder used for crystal growth. Moreover, we emphasize the importance of employing higher-purity starting materials and exploring the possibility of reducing the dopant concentration, provided that such a reduction does not significantly degrade the detector's light yield, as suggested, for example, in Ref. [20].

New limits have been set on five distinct decay channels of ^{84}Sr: the two-neutrino (2ν) and the neutrinoless (0ν) modes for $\epsilon\beta^+$ and 2ϵ processes, targeting both the ground state (0^+) and the first excited level (2^+ at 881.6 keV) of the daughter nucleus ^{84}Kr. Thanks to the low-background environment and set-up, and to the realized SrI_2(Eu) crystal scintillator, the effective "source=detector" approach, generally offering higher efficiency for detection of 2β decays (up to 100%), has been exploited. This has contributed to the significant improvements of the limits determined in the present measurement.

This work also demonstrates that there is considerable potential for further improvement in producing radiopure, relatively large SrI_2(Eu) crystals through optimized selection, purification, and growth protocols, making them promising for the search for various rare processes.

Acknowledgements This work was supported by the INFN Grant 73/Rebus awarded to F.C.; the experimental activities for crystal qualifications and related results were conducted within the framework of the DAMA installations and activities. F.C. would also like to acknowledge Serge S. Nagorny (GSSI, Aquila) for scientific discussions about ^{87}Rb contamination in SrI_2(Eu) crystal scintillators.

Funding Open access funding provided by Università degli Studi di Roma Tor Vergata within the CRUI-CARE Agreement.

Data availability statement This manuscript has no associated data. [Author's comment: The data produced in this study are contained in the publication].

Code availability statement This manuscript has no associated code/software. [Author's comment: Code/Software sharing not applicable to this article as no code/software was generated or analysed during the current study].

A Appendix: Scintillation decay time

The scintillation decay time is a fundamental property of scintillator materials, directly affecting their temporal resolution and suitability for various detection applications [7,9–12]. In SrI_2(Eu), the emission is predominantly governed by the $5d \rightarrow 4f$ transitions of the Eu^{2+} activator ion [21,22].

The decay time of the SrI_2(Eu) crystal was characterized through a systematic analysis of pulse shapes in the energy range of 600–1000 keV, and selecting events with t_m within 2σ from t_m^0. The averaged pulse shape was then fitted (see Fig. 10) using a triple-exponential decay function of the form:

$$f(t) = A_1 e^{-t/\tau_1} + A_2 e^{-t/\tau_2} + A_3 e^{-t/\tau_3} \quad \text{(A.1)}$$

Here, A_i represents the amplitude of each component (with negative values corresponding to the inverted pulse polarity), and τ_i denotes the corresponding decay time constant. The

Table 6 Decay time components of the SrI_2(Eu) scintillation light

Component	Amplitude A	Decay time τ [ns]	Relative contribution [%]
Very fast	−0.184(6)	93(3)	0.4
Fast	−0.114(6)	316(12)	0.9
Slow	−1.0832(4)	3847.1(15)	98.7

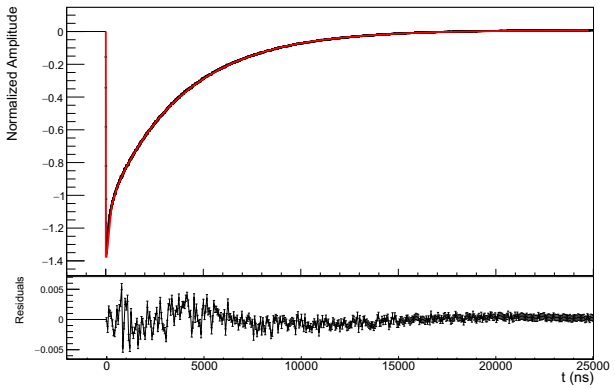

Fig. 10 Top: Average pulse shape with superimposed the exponential fit with three components performed on an area-normalized sample of 1000 pulses from events between 600 and 1000 keV. Bottom: residuals from the comparison of the two above behaviours

baseline offset was treated as a free parameter during the fitting procedure.

The fit yielded three distinct temporal components, summarized in Table 6. The dominant contribution to the scintillation light output originates from the slow component, with a decay time constant of $\tau_3 = 3.8471(15)$ μs, accounting for approximately 98.7% of the total signal. Two minor components were identified: a fast component with $\tau_2 = 316(12)$ ns contributing 0.9% of the signal, and a very fast component with $\tau_1 = 93(3)$ ns representing 0.4% of the total light yield. The quality of the fit, assessed through a reduced chi-squared value corresponds to $\chi^2/\text{NDF} \approx 0.81$.

The presence of multiple decay components indicates complex excitation and relaxation dynamics within the crystal, potentially arising from radiative recombination at different Eu^{2+} sites or from defect-related emission. The primary decay component, on the microsecond scale, is consistent with the spin-forbidden nature of the $5d \rightarrow 4f$ transition in divalent europium [21,22].

References

1. R. Hofstadter, "Europium activated strontium iodide scintillators," U.S. Patent, vol. No. 3,373,279, 1968
2. M. Cody et al., Strontium iodide scintillators for high energy resolution gamma ray spectroscopy. Proc. of SPIE **7079**, 707917 (2008)
3. N. Cherepy et al., Strontium and barium iodide high light yield scintillators. Appl. Phys. Lett. **92**(8), 083508 (2008)
4. E. van Loef et al., Crystal Growth and Scintillation Properties of Strontium Iodide Scintillators. IEEE Trans. Nucl. Sci. **56**, 869 (2009)
5. J. Glodo et al., Concentration Effects in Eu Doped SrI_2. IEEE Trans. Nucl. Sci. **57**, 1228 (2010)
6. M. Alekhin et al., Scintillation properties and self absorption in SrI_2:Eu^{2+}. IEEE Trans. Nucl. Sci. **58**, 2519 (2011)
7. P. Belli et al., Radioactive contamination of SrI_2(Eu) crystal scintillator. Nucl. Inst. and Meth. A **670**, 10 (2012)
8. A. Giaz et al., Preliminary investigation of scintillator materials properties: SrI_2:Eu, $CeBr_3$ and GYGAG: Ce for gamma rays up to 9 MeV. Nucl. Inst. and Meth. A **804**, 212 (2015)
9. K. Yang et al., Scintillation kinetics and thermoluminescence of SrI_2:Eu^{2+} single crystals. J. of Luminescence **132**, 1824 (2012)
10. K. Nishimoto et al., Eu concentration dependence on scintillation properties of Eu doped SrI_2 single crystals grown by modified micro-pulling-down method. Opt. Mater. **36**, 1946–1949 (2014)
11. K. Nishimoto et al., "Corrigendum to "Eu concentration dependence on scintillation properties of Eu doped SrI_2 single crystals grown by modified micro-pulling-down method"[opt. mater. 36/12 (2014) 1946-1949]," Optical Materials, vol. 45, p. 258, 2014
12. R. Hawrami et al., Bridgman bulk growth and scintillation measurements of SrI_2:Eu^{2+}. J. Cryst. Growth **379**, 69 (2013)
13. H. Zhu et al., Bridgman Method for Growing Metal Halide Single Crystals: A Review. Inorganics **13**(2), 53 (2025)
14. R. Bernabei, The DAMA Project: Technical Developments, Experiments and Results. Int. J. Mod. Phys. A **31**, 1642001 (2016)
15. S. Agostinelli et al., Geant4 - a simulation toolkit. Nucl. Instr. Meth. A **506**, 250 (2003)
16. J. Meija et al., Isotopic compositions of the elements 2013. Pure Appl. Chem. **88**, 293 (2016)
17. Z. Ge et al., High-precision measurement of the atomic mass of ^{84}Sr and implications to isotope shift studies. Eur. Phys. J. A **60**, 147 (2024)
18. O. Ponkratenko et al., Event generator DECAY4 for simulating double-beta processes and decays of radioactive nuclei. Phys. At. Nucl. **63**, 1282 (2000)
19. G.J. Feldmann, R.D. Cousins, Unified approach to the classical statistical analysis of small signals. Phys. Rev. D **57**, 3873 (1998)
20. A. Smerechuk et al., Growth and scintillation performances of SrI_2: Eu with low activator concentration. J. Cryst. Growth **521**, 41–45 (2019)
21. P. Dorenbos, The 5d level positions of the trivalent lanthanides in inorganic compounds. J. of Luminescence **91**(3–4), 155–176 (2000)
22. T. Kawai et al., Luminescence properties of pure and Eu-doped SrI_2 crystals purified by a Liquinert process and grown by vertical Bridgman method. J. Lumin. **176**, 58 (2016)